Supplementary Information
For

Restructuring of emergent grain boundaries at free surfaces – an interplay between core stabilization and elastic stress generation

Xiaopu Zhang,[1*] Mengyuan Wang,[2] Hailong Wang,[2*] Moneesh Upmanyu,[3*] John J. Boland[1*]

[1]Centre for Research on Adaptive Nanostructures and Nanodevices (CRANN), AMBER SFI Research Centre and School of Chemistry, Trinity College Dublin, Dublin 2, Ireland

[2]CAS Key Laboratory of Mechanical Behavior and Design of Materials, Department of Modern Mechanics, University of Science and Technology of China, Hefei, Anhui 230027, People's Republic of China

[3]Group for Simulation and Theory of Atomic-Scale Material Phenomena (stAMP), Mechanical and Industrial Engineering, Northeastern University, Boston, MA 02115, USA

This document contains Supplementary Figures (1-13), Supplementary Notes (1-3), Supplementary Table (1-5) and Supplementary references (1-5).

Contents

Supplementary Note

Note SI-1: Scanning tunnelling microscopy and spectroscopy

STM topography image obtained with U = -1 V and It = 200 pA on nanocrystalline copper films is shown in Fig. SI-1a. It shows the triple junction of eGB26 on the top right corner. We draw a line away from TJ and show in Fig. SI-1b the spectra recorded at different locations away from the TJ. These data show the presence of additional states around 0.5 V above the Fermi surface at the TJ location, which are different from that on a free surface, possibly due to hybridization of surface states and bulk states[1,2]. To check the effect of density of states, we also scanned the same area of the bicrystal with difference biases, shown in Fig. SI-1c. There is additional corrugation seen at ~ 0.5V, which is consistent with the spectra results on NC copper films. Hence to determine an accurate groove shape, we collected images with sample biases lower than 0.5V to avoid this electronic effect.

Note SI-2: Framework for energetic analysis

To test the formation and stability of rotated crystal, we perform an energetic analysis of a valley formed at an eGB based on the scheme outline in Fig. 3b. Figure SI-9 shows two equivalent pathways for realizing the out-of-plane rotation φ of a surface layer of thickness h, driven by the $\langle 111\rangle \rightarrow \langle 112\rangle$ rotation of the misorientation axis within the grain boundary plane. The rotated layer preserves its commensurability with the rest of the crystal, and this is achieved by mating it to the rest of the crystal (Fig. SI-9c) or by introducing a V-shaped notch with included angle φ and thickness h_0, and using shear stresses to stitch it at the grain boundary (Fig. SI-9b). The latter forms the basis for our computational scheme shown in Fig. 3b.

Using the initial unrotated bicrystal as the reference, the total energy change (per unit grain boundary width) can be expressed as

$$\Delta U = \Delta U_{GB} + \Delta U_s + \Delta U_{TJ} + \Delta U_e \ , \qquad [S1]$$

where ΔU_{GB} is the change in the grain boundary energy, ΔU_{TJ} is the change in triple junction energy at the emergent grain boundary, ΔU_s is the change in surface energy associated with elimination of film surface following the stitching operation, and ΔU_e the elastic energy stored within the rotated bicrystal to bring it into commensuration with the remainder of the bicrystal.

Grain boundary energy: The driving force for the rotation follows from the geometry of the rotation and the depth of the rotated bicrystal h (in general, distinct from the prescribed thickness h_0). Denoting $\gamma_{[112]}$ and $\gamma_{[111]}$ as the bulk grain boundary energies (sans surface) within the rotated and unrotated (reference) bicrystals corresponding to the grain boundary inclination, the energy change follows from the change in both the grain boundary energy and area,

$$\Delta U_{GB} = \gamma_{112} \frac{h}{\cos(\varphi/2)} - \gamma_{111} h \ . \qquad [S2]$$

Note that the contribution of the grain boundary energy change to the driving force for rotation is $\frac{\gamma_{112}}{\cos \varphi/2} - \gamma_{111}$.

Surface energy: The contribution is based on the surface area eliminated by shear-stitching the notch,

$$\Delta U_s = -\gamma_s \left[2h \tan\left(\frac{\varphi}{2}\right)\right], \qquad \text{[S3]}$$

where γ_s is the energy of the $\langle 111 \rangle$ film surface. For simplicity, we ignore higher order corrections due to surface stresses and related surface reconstructions.

Triple junction energy: The change in energy of the surface TJ before and after the rotation $\Delta U_{TJ} = U_{TJ}^{112} - U_{TJ}^{111}$ is extracted using MS simulations within computational cells consisting of 2 GBs and the relaxed [111] free surfaces subject to in-plane periodic boundary conditions, as shown in Fig. SI-7. The energy of the TJ within each computational cell is

$$U_{TJ}^{112}, U_{TJ}^{111} = \frac{U - 4U_s L_x L_y - 2U_{GB} L_z L_X}{4L_x} \ ,$$

where U is the total energy of the system, $L_x,\ L_y,\ L_z$ are the dimensions of the configuration in three directions, U_s is the [111] surface energy, and U_{GB} is the corresponding grain boundary energy. Table SI-2 summarizes the results of the TJ energy calculations. The changes in TJ energies are $\Delta U_{TJ} = 0.0038$ nJ/m and -0.0010 nJ/m for the eGB26 and eGB3.89 systems, respectively. They are negligible compared to the changes in the bulk GB and surface energies and therefore this contribution is ignored for the remainder of the analysis.

Elastic energy: To quantify the elastic energy stored within the rotated and reference regions, we employ a combination of finite element method (FEM)-based continuum simulations (Methods) and dimensional analyses. Figure SI-11 shows the details of the computational cell employed to extract the stress field associated with stitching together a V-shaped surface notch of thickness h and included angle φ. Stresses are applied along the layer on each side of the notch until it vanishes. Unlike the atomic-scale simulations, the stitched notch yields a perfect yet stressed crystal rather than a rotated bicrystal. As such, the continuum computations ignore the corrections to the stress field, if any, due to stress accommodations at the grain boundary that forms as the notch is eliminated.

The elastic displacement fields are plotted in Fig. SI-12. The horizontal displacement field decays almost radially away from emergent grain boundary, resulting in tensile stresses on the film surface, while the vertical displacement exhibits a tear-drop profile around the grain boundary. For linear elastic displacements and stresses and for an infinitely thick film $h/H \ll 1$, we expect the elastic energy per unit grain boundary width to scale quadratically with the height of the notch ($\sim G\ h^2$) and the strain ($\sim \varphi^2$), that is

$$\Delta U_e = C\ G\varphi^2 h^2 \ , \qquad \text{[S4]}$$

with C a material constant. We have validated the variation by performing FEM simulations for notches with varying h and φ. Figure SI-12a shows the elastic energy $\Delta U_e / Gh^2$ plotted as a function of φ. The scaling is well-described by a quadratic fit with a Poisson's ratio dependent material constant, $C \equiv C(\nu) = 0.1224$.

For finite thickness of the reference crystal, the elastic energy partitions differently between the rotated and reference crystals and is therefore modified. To a leading order, the elastic field scales with h for the same height ratio, h/H. Then, the elastic energy can be expressed as,

$$\Delta U_e = f\left(\frac{h}{H}\right)\ C\ G\varphi^2 h^2, \ \ f\left(\frac{h}{H}\right) = 1 + A_1 \exp\left(-\frac{B_1 H}{h}\right) + A_2 \exp\left(-\frac{B_2 H}{h}\right) \qquad \text{[S5]}$$

where the finite thickness effect is captured by the function $f(h/H)$. Figure SI -12b shows the

correction to the elastic energy within the FEM simulations, plotted as the extracted value of $f(h/H)$ for varying thickness ratios, h/H. Again, the elastic energy correction is in excellent agreement with the exponential dependence on the thickness ratio (Eq. S5).

Note SI-3: Valley formation and stability

Energetic analysis: Combining Eqs. S1-S5, the total energy associated with the relaxation of the emergent grain boundary via rotation into a valley can be expressed as

$$\Delta U(h) = -2\gamma_s \left[h \tan\left(\frac{\varphi}{2}\right)\right] + \left(\frac{\gamma_{[112]}}{\cos\left(\frac{\varphi}{2}\right)} - \gamma_{[111]}\right) h - f\left(\frac{H}{h}\right) C\, G\varphi^2 h^2 , \qquad [S6]$$

where the linear term captures the changes in the surface and grain boundary energies, while the quadratic term is the elastic energy contribution. Minimization of $\Delta U(h)$ yields the equilibrium thickness h^* of the rotated layer that stabilizes the valley.

Below, we perform the minimization for the two $\langle 111 \rangle$ symmetric tilt grain boundaries: a $\theta = 26.008^{\circ}$ HAGB and a $\theta = 3.890^{\circ}$ LAGB. The energy change is quantified using values extracted from atomic-scale simulations for a $H = 50$ nm thick film (Tables SI 3 and 4). For both bicrystals we take the surface energy to be $\gamma_s = 1.239\ \mathrm{J/m^2}$ and the material constant $C = 0.1224$. The equilibrium thickness of the rotated layer h^* and the energy change for both eGB systems extracted in the continum and atomic-scale computations are summarized in Tab. SI-5.

eGB26 system: The misorientation axis rotation that minimizes the GB energy for a misorientation $\theta = 26.008^{\circ}$ is associated with an out-of-plane rotation of $\varphi = 9.097^{\circ}$. The grain boundary energies (enthalpies) before and after rotation are (see Methods): $\gamma_{111} = 0.833\ \mathrm{J\ m^{-2}}$ and $\gamma_{112} = 0.721\ \mathrm{J\ m^{-2}}$. The rotated layer thickness dependence of the surface, grain boundary and elastic energies are plotted in Fig. 4d. The energy minimization yields $h^* = 1.000$ nm with $\Delta U^* = -0.1536\ \mathrm{nJ/m}$, which corresponds to a little less than six $\langle 111 \rangle$ layers with the FCC crystal. Atomic simulation of the relaxed bicrystal with rotation limited to the top five layers yields an enthalpy of $\Delta U^* = -0.0954\ \mathrm{nJ/m}$, in good agreement with the continuum predictions.

eGB3.89 system: The $\theta = 3.890^{\circ}$ grain boundary exhibits an energy minimizing out-of-plane rotation of $\varphi = 1.375^{\circ}$, with $\gamma_{111} = 0.289\ \mathrm{J\ m^{-2}}$ and $\gamma_{112} = 0.219\ \mathrm{J\ m^{-2}}$ (Table SI-3). The thickness dependence of the surface, grain boundary and elastic energies are plotted in Fig. 5b, and they together yield an equilibrium rotated layer thickness of $h^* = 13.131$ nm with $\Delta U^* = -0.676\ \mathrm{nJ/m}$. As a comparison, the enthalpy extracted within the atomic-scale simulations is $\Delta U^* = -0.513\ \mathrm{nJ/m}$.

Infinite thickness limit: Taking the $H/h \gg 1$ ($f = 1$) limit for the energy change functional, we get

$$h^* = \frac{\gamma_{111} - \gamma_{112}/\cos(\varphi/2) + 2\gamma_s \tan(\varphi/2)}{2C\, G\varphi^2} . \qquad [S7]$$

The equilibrium values for the LAGB and HAGB are $h^* = 1.000$ nm and $h^* = 14.211$ nm, respectively, with corresponding values of $\Delta U^* = -0.1536\ \mathrm{nJ/m}$ and $\Delta U^* = -0.708\ \mathrm{nJ/m}$. As expected, increasing film thickness has a negligible effect on the thickness of the rotated layer for the HAGB as the rotated layer less than a nanometer thick for $H = 50$ nm.

Vanishing out-of-plane rotation limit: For $\varphi \to 0$, the surface contribution becomes negligible $\left[\tan\left(\frac{\varphi}{2}\right) \to 0\right]$ and the grain boundary contribution is simply the difference between the

energies of the rotated and unrotated grain boundaries $\left[\cos\left(\frac{\varphi}{2}\right) \to 1\right]$. Then, Eq. S7 simplifies to

$$h^* = \frac{(\gamma_{111} - \gamma_{112})}{2C\,G\varphi^2}. \qquad [S7]$$

Supplementary Figure

Figure SI-1 Scanning tunneling microscopy and spectroscopy

(a) STM topography image obtained with U = -1 V and I_t = 200 pA on nanocrystalline copper film at eGB26. (b) Four dI/dV curves taken along the line in (a) away from the triple junction. Modulation bias and frequency are 15 mV and 1066 Hz, respectively. (c) Topographic profile of the eGB26 TJ groove in the bicrystal recorded along the cross section in Fig. 2b at different bias together with the profile of the TJ groove at the eGB26 nanocrystalline sample.

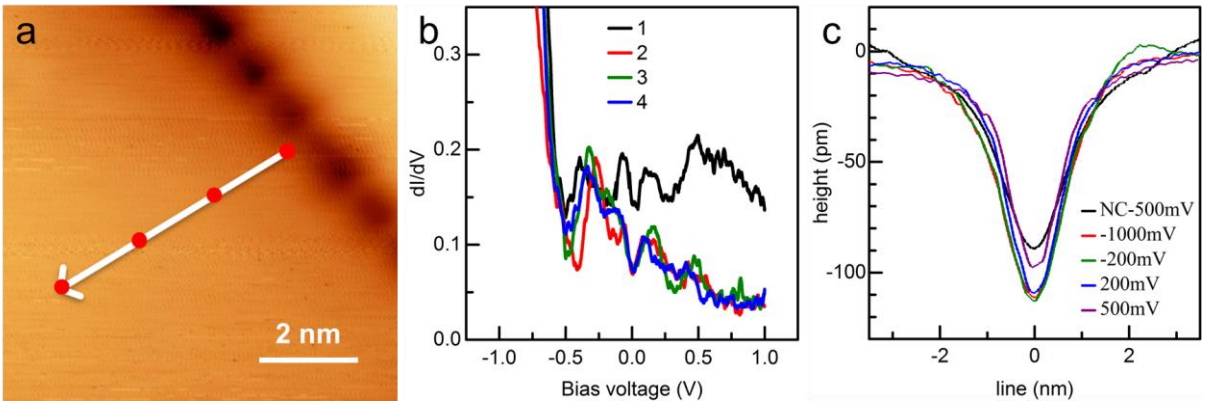

Figure SI-2 Geometrical specification

(a) Symmetric tilt grain boundary with tilt axis $[\mathbf{111}]$, angle $\boldsymbol{\theta = 26.01°}$, and boundary normal y, created by rotating the median lattice by $\pm\boldsymbol{\theta/2}$ along $[\mathbf{111}]$ into black and white crystals, respectively. (b) Rotating the black and white crystals by $\pm\boldsymbol{\varphi/2}$ along $[\mathbf{\bar{1}\bar{1}2}]$ in the median lattice respectively.

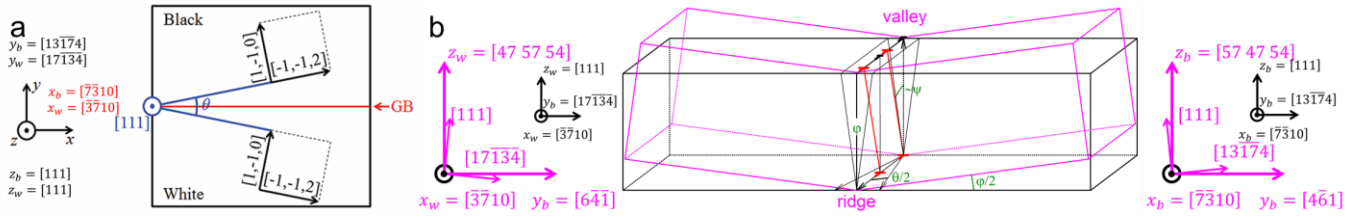

Figure SI-3 Calculated boundary energies in bulk

(a). Calculated energy of two symmetric tilt boundaries with mean boundary plane $(1\bar{1}0)$ and $(11\bar{2})$, shown as black and red, respectively. Green line corresponds to the calculated [112] boundary energy as a function of in-plane angle. (b). Calculated boundary energy as the composite rotation axes shift away from [111] for a range of in-plane angles from 32.20° to 60°. (c) Calculated energy variation between [111] boundary and corresponding [112] boundary and its variation ratio. (d) Comparison of the line profile in experiment shown in Fig. 1(c) and that of (111) plane at a boundary in bulk with tilt axis [112].

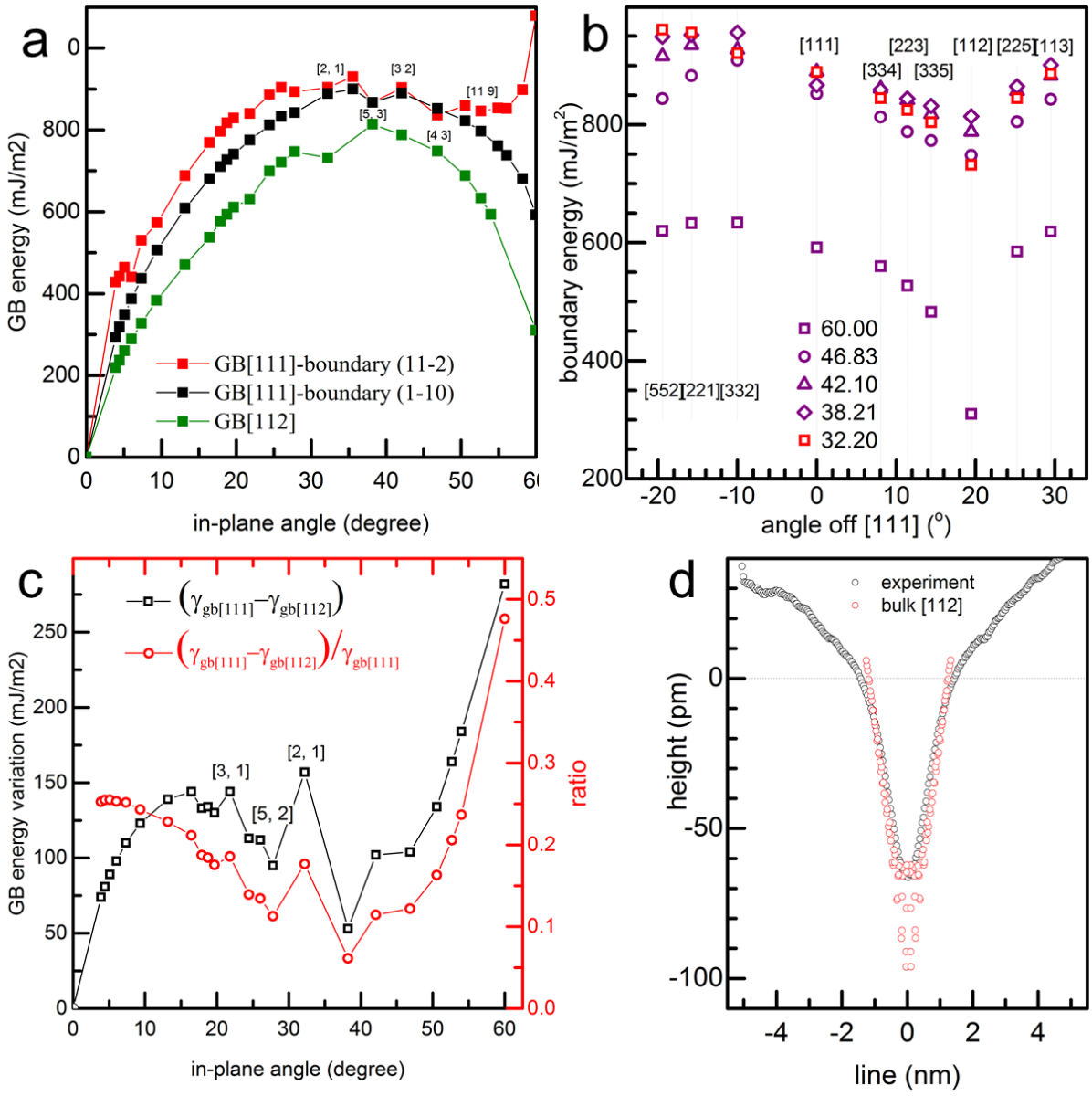

Figure SI-4 Atomic-simulation of unrotated eGB26 system

Atomic-scale configuration of the equilibrated eGB26 system comprised of the [111] - $\theta = 26.1°$ symmetric tilt HAGB terminating at the surface of an $H = 50$ nm thick [111] copper film. (a, top and bottom) Top and side view of the bicrystal with the orientations of the grains as indicated. The color indicates atomic (virial) stress. (b) The atomic configuration of the surface triple junction showing the repeat structural units and the periodicity vector. The atoms are colored based on their depth coordinate. (c) Line profile (solid black) and its slope (solid green) across one of the groove minima indicated in (b) (dashed white line).

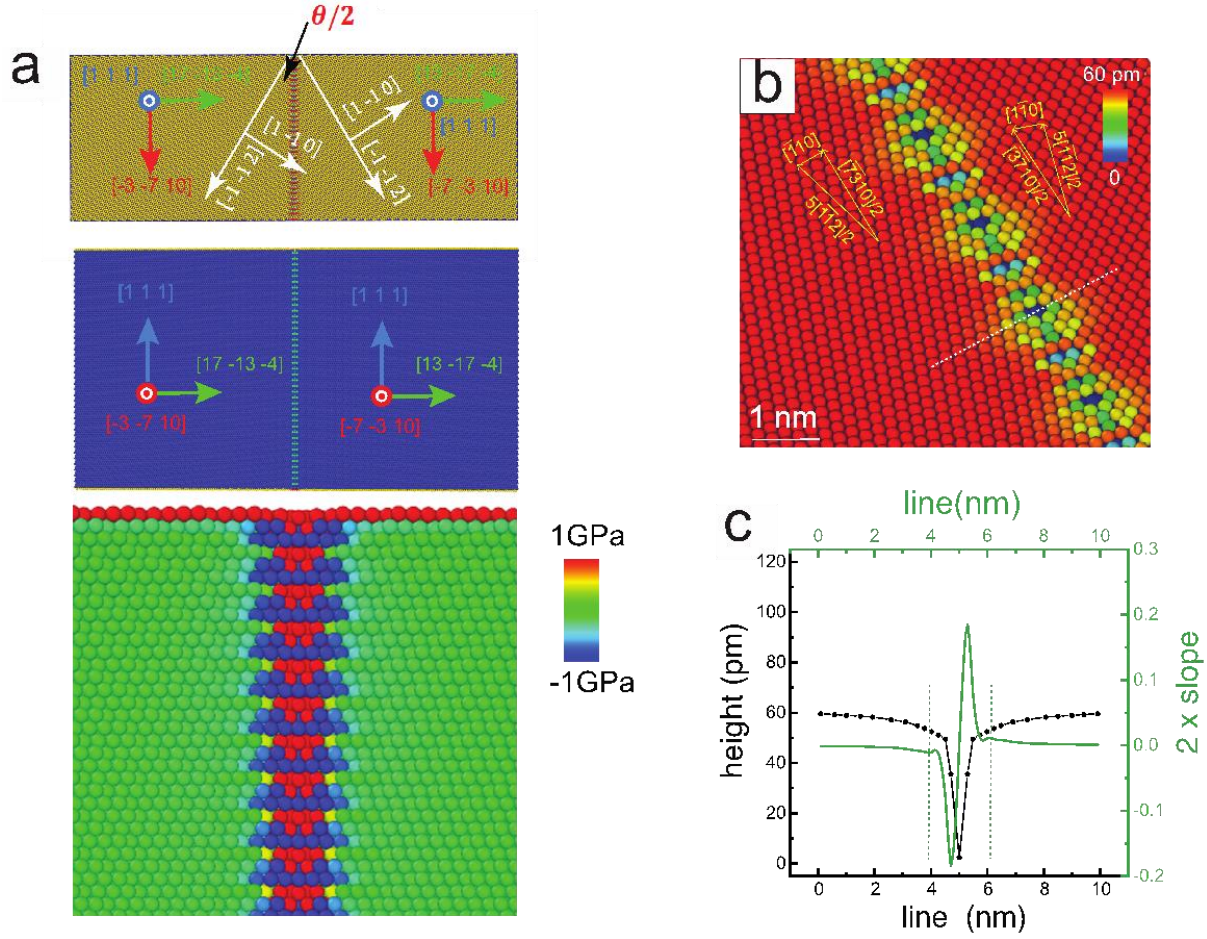

Figure SI-5 Computational cell for the rotated eGB26 system

Atomic-scale simulation cell with (a) in-plane rotation θ and (b) out-of-plane rotation φ associated with (c) the tilting of the misorientation axis ψ of the eGB26 system and the formation of a coupled valley-ridge at the two free surfaces.

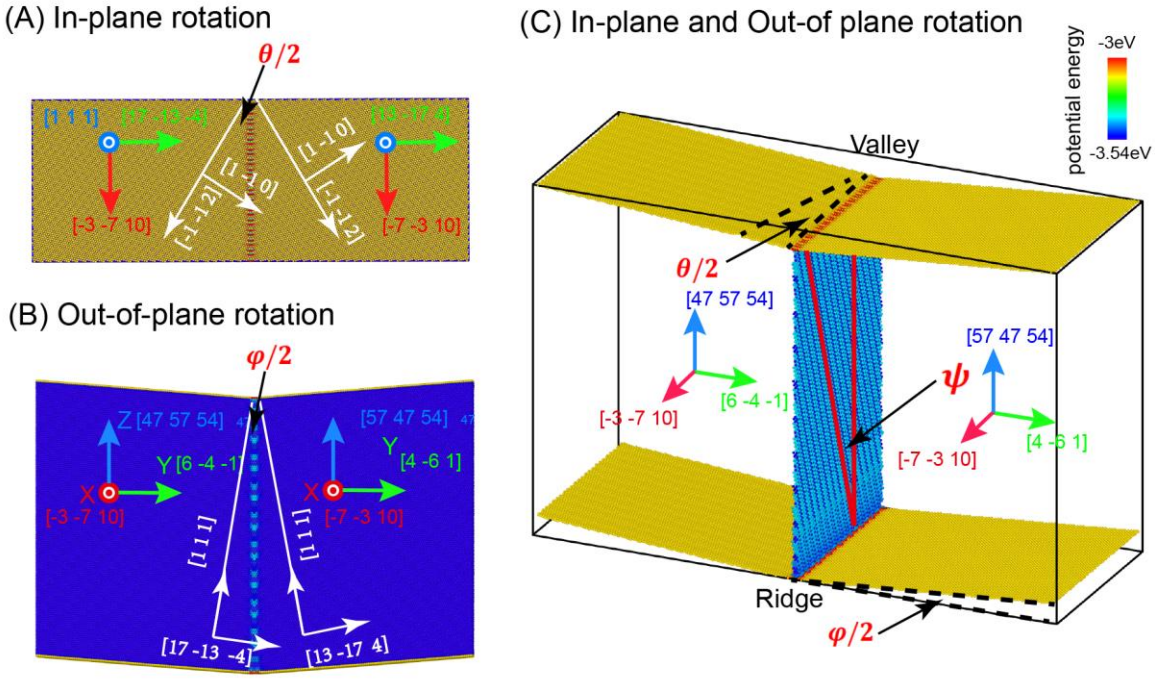

Figure SI-6 Configurations of the rotated and mechanically constrained eGB26 system

Effect of out-plane rotation and mechanical constraint on the surface TJ structure for an equilibrated eGB26 system. (left) The reference unrotated eGB, (middle) the eGB with an out-of-plane rotation of φ, and (right) the rotated and reoriented eGB. Atoms are colored based on their potential energy.

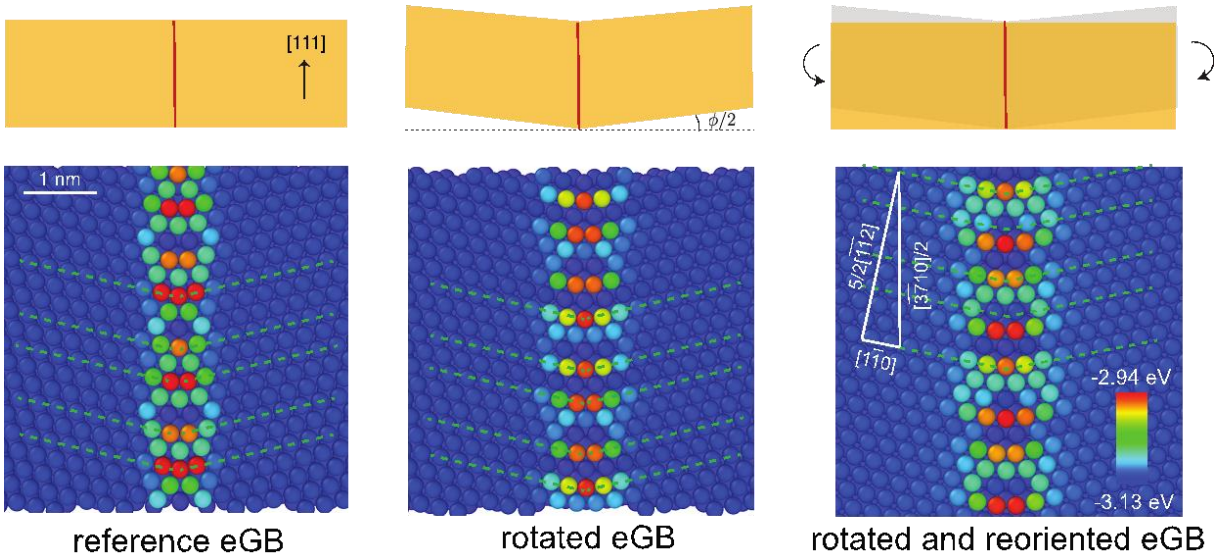

Figure SI-7 Computational scheme for calculations of surface TJ energies

The atomic simulation cells for calculations of TJ energies before (left) and after (right) the rotation of the eGB26 system. The atoms are colored based on their potential energies.

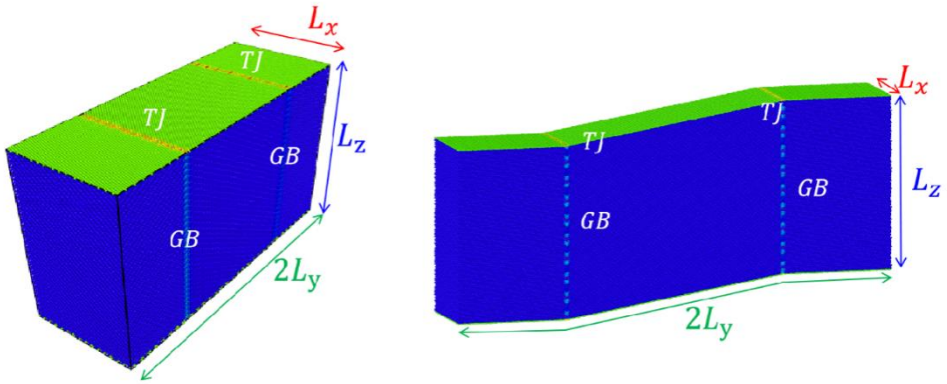

Figure SI-8 Effect of the film thickness on the surface profiles for the eGB26 system

Effect of the film thickness H on the surface profiles for the eGB26 system extracted using MS simulations.

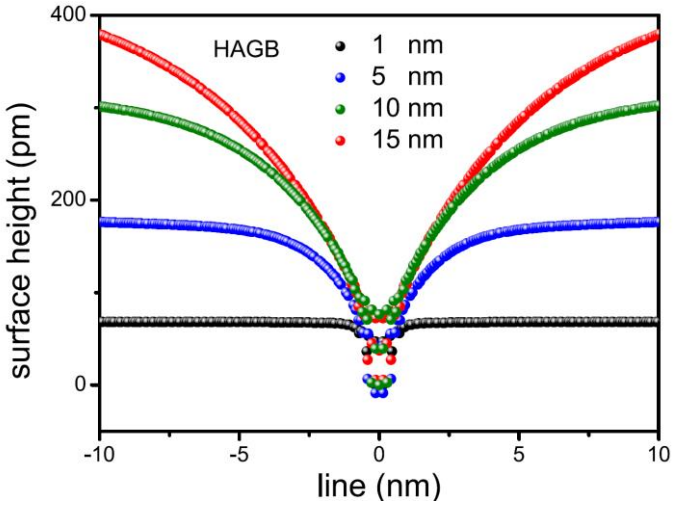

Figure SI-9 Computational framework for studying partially rotated eGBs

Computational scheme for GB relaxation on surface using two strategies: surface notch followed by shear as shown in the main text (Fig. 3b), or surface notches at the edges followed by rotation to the substrate.

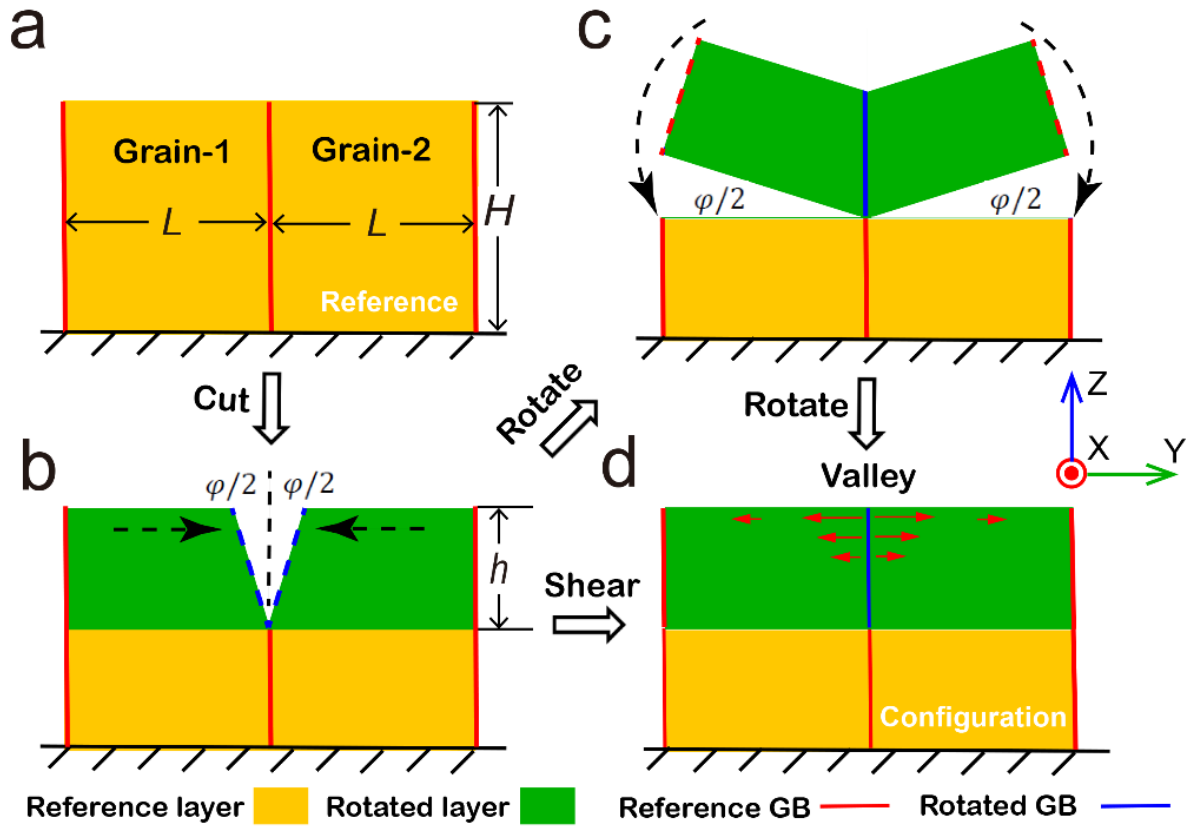

Figure SI-10 Surface profiles for varying rotated layers depth for the eGB26 system.

Surface profiles averaged over groove minima for varying depths of the rotated layers within a $H = 50$ nm thick film for the eGB26 system.

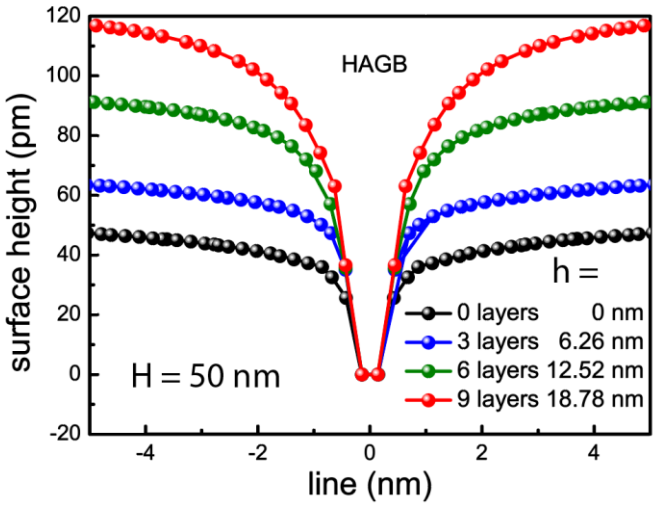

Figure SI-11 FEM computational cell for elastic deformations at an eGB valley

(left) Finite element method computational cell with a V-shaped notch and fixed boundary conditions. (a, b) Contour plots of scaled (a) horizontal and (b) vertical absolute displacements $|u_y|/u_y^{max}$ and $|u_z|/u_z^{max}$ respectively, normalized by their maximum absolute values u_y^{max} and u_z^{max}. Colors (blue to red) represent low to high displacements.

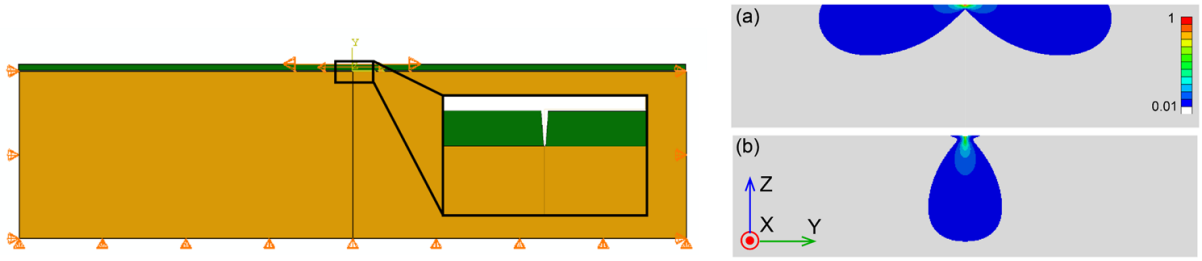

Figure SI-12 FEM computed thickness-dependent elastic energies

(a) The computed elastic energy $\Delta U_e/Gh^2$ as a function of φ, and its power fit to the form $\Delta U_e/Gh^2 = C\varphi^n$. (b) The correction to the elastic energy, $f(h/H)$ as a function of thickness ratio h/H and an exponential fit of the form $f(h/H) = 1 + A_1 \exp(-B_1(H/h)) + A_2 \exp(-B_2(H/h))$. See Supplementary Notes for details.

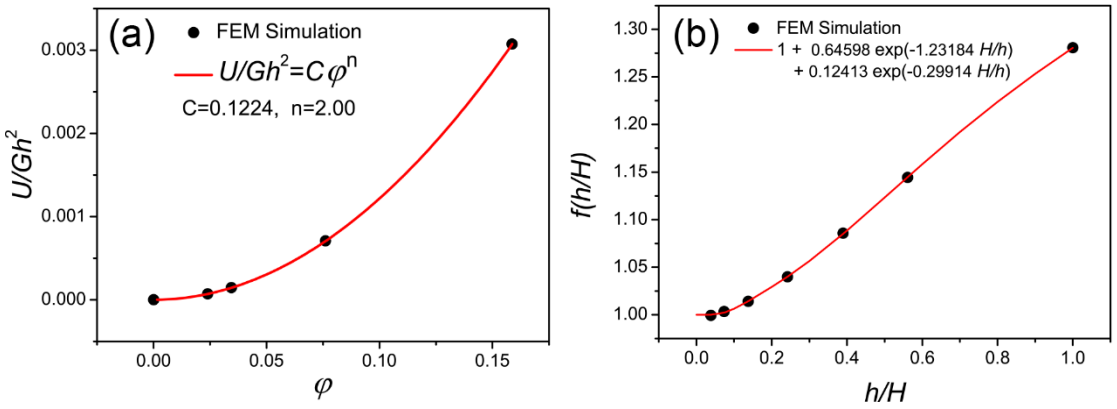

Figure SI-13 Same as in Fig. SI-6, but for the eGB3.89 system

Same as in Fig. SI-6, but for the eGB3.89 system.

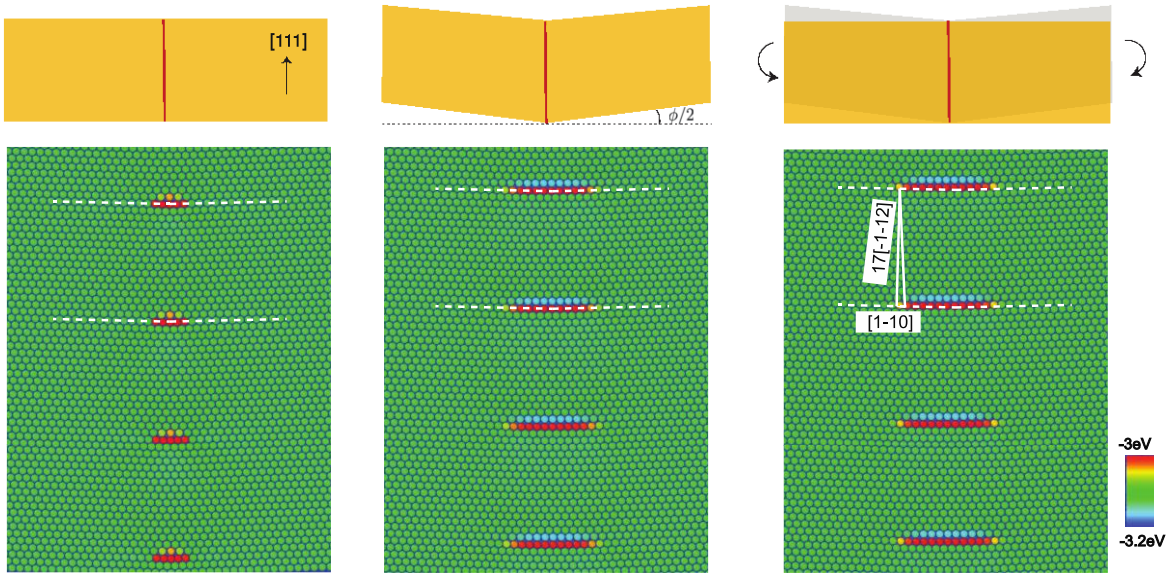

Supplementary Table

Table SI-1. Geometry and size of the bicrystal eGB simulation cells

The computational cell geometries and size used in the atomistic simulations of the eGB26 and eGB3.89 systems. P_x, P_y, and P_z denote the crystal orientations along the x, y and z directions respectively. See Fig. SI-4~5 for details.

θ(°)	φ(°)	P_x	P_y	P_z	ψ(°)
26.008	0	[-3 -7 10]	[17 -13 -4]	[1 1 1]	0
	0	[-7 -3 10]	[13 -17 4]	[1 1 1]	0
26.008	9.097	[-3 -7 10]	[6 -4 -1]	[47 57 54]	19.471
	9.097	[-7 -3 10]	[4 -6 1]	[57 47 54]	19.471
Cell size		9.1 nm	50 nm	50.1 nm	
3.890	0	[-8 -9 -17]	[26 -25 -1]	[1 1 1]	0
	0	[-9 -8 17]	[25 -26 1]	[1 1 1]	0
3.890	1. 375	[-8 -9 -17]	[35 -33 -1]	[570 587 579]	19.471
	1.375	[9 8 -17]	[33 -35 1]	[587 570 579]	19.471
Cell size		15.1 nm	100.1 nm	50.1 nm	

Table SI-2. Computed triple junction energies

Triple junction energies calculated using MS simulations of the computational cell geometry shown in Fig. SI- 4.

	$U_{TJ}^{<111>}(\mathrm{nJ/m})$	$U_{TJ}^{<112>}(\mathrm{nJ/m})$	$\Delta U_{TJ}(\mathrm{nJ/m})$
LAGB	-0.07515	-0.07610	-0.0010
HAGB	-0.07512	-0.07134	0.0038

Table SI-3. Physical parameters of pure copper employed for continuum analyses

Physical parameters for pure copper obtained using atomic-scale (molecular statics) simulations, including those reported in prior studies[3,4].

Cohesive energy (u_c)	-3.54 eV/atom
Elastic modulus (G)	128.500 GPa
Shear modulus (G)	47.762 GPa
Surface energy (γ_s)	$1.239\ \mathrm{J/m^2}$
Poisson's ratio (ν)	0.345

Table SI-4. Mechanical properties for pure copper employed for continuum analyses

Mechanical properties for pure copper along horizontal and vertical directions obtained using atomic-scale (molecular statics) simulations.

Crystal orientation	Elastic modulus $E(\mathrm{GPa})$	Poisson ratio ν	Shear modulus $G(\mathrm{GPa})$
Polycrystalline average	128.500	0.345	47.762
HAGB horizontal [17 -13 -4]	137.216	0.225	56.006
HAGB vertical [1 1 1]	181.550	0.267	71.646
LAGB horizontal [26 -25 -1]	134.587	0.224	54.978
LAGB vertical [1 1 1]	181.550	0.267	71.646

Table SI-5. Parameter set used in the FEM computations

The parameter set used in the continuum computations and the corresponding equilibrium thickness h^* and energy of the two eGB systems. The results of the atomic-scale computations are also tabulated for comparison.

Crystal orientation	Elastic modulus E (GPa)	Poisson's ratio ν	Shear modulus G (GPa)	$C(\nu)$	Equilibrium thickness $h^*\ (nm)$	Energy change ΔU^* (nJ/m)
HAGB (polycrystalline average)	128.500	0.345	47.762	0.1227	1.000	-0.1536
eGB26 horizontal [17 -13 -4]	137.216	0.225	56.006	0.1080	1.007	-0.1547
eGB26 normal [1 1 1]	181.550	0.267	71.646	0.1141	0.745	-0.1144
eGB26 atomic-scale simulations	/	/	/		1.25	-0.0954
eGB3.89 (polycrystalline average)	128.500	0.345	47.762	0.1227	13.131	-0.676
eGB3.89 horizontal [26 -25 -1]	134.587	0.224	54.978	0.1122	12.975	-0.668
eGB3.89 normal [1 1 1]	181.550	0.267	71.646	0.1187	9.676	-0.493
eGB26 atomic-scale simulations	/	/	/		14.4	-0.513

Supplementary References

1 Christiansen, J. *et al.* Atomic-scale structure of dislocations revealed by scanning tunneling microscopy and molecular dynamics. *Phys Rev Lett* **88**, 206106, doi:10.1103/PhysRevLett.88.206106 (2002).

2 Heidorn, S. & Morgenstern, K. Spatial variation of the surface state onset close to three types of surface steps on Ag(111) studied by scanning tunnelling spectroscopy. *New J Phys* **13**, doi:Artn 033034

10.1088/1367-2630/13/3/033034 (2011).

3 Mishin, Y., Mehl, M. J., Papaconstantopoulos, D. A., Voter, A. F. & Kress, J. D. Structural stability and lattice defects in copper: Ab initio, tight-binding, and embedded-atom calculations. *Phys Rev B* **63**, 224106, doi:ARTN 224106

DOI 10.1103/PhysRevB.63.224106 (2001).

4 Rassoulinejad-Mousavi, S. M., Mao, Y. J. & Zhang, Y. W. Evaluation of copper, aluminum, and nickel interatomic potentials on predicting the elastic properties. *J Appl Phys* **119**, doi:Artn 244304 10.1063/1.4953676 (2016).

5 Zhang, X. *et al.* Nanocrystalline copper films are never flat. *Science* **357**, 397-400, doi:10.1126/science.aan4797 (2017).